Biosensors and Bioelectronics 144 (2019) 111665

Contents lists available at ScienceDirect

Biosensors and Bioelectronics

journal homepage: www.elsevier.com/locate/bios

In vivo monitoring of superoxide anion from Alzheimer's rat brains with functionalized ionic liquid polymer decorated microsensor

Qiwen Peng[a,b], Xueyan Yan[a,b], Xinran Shi[a,b], Shanshan Ou[a,b], Hui Gu[c], Xiaoxing Yin[a,**], Guoyue Shi[d], Yanyan Yu[a,b,*]

[a] *Jiangsu Key Laboratory of New Drug Research and Clinical Pharmacy, Xuzhou Medical University, 209 Tongshan Road, Xuzhou, 221004, Jiangsu, PR China*
[b] *Department of Pharmaceutical Analysis, School of Pharmacy, Xuzhou Medical University, 209 Tongshan Road, Xuzhou, 221004, Jiangsu, PR China*
[c] *School of Chemistry and Chemical Engineering, Hunan University of Science and Technology, Xiangtan, Hunan, 411201, PR China*
[d] *Department of Chemistry, School of Chemistry and Molecular Engineering, East China Normal University, 500 Dongchuan Road, Shanghai, 200241, PR China*

ARTICLE INFO

Keywords:
Functionalized PIL
$O_2^{\bullet -}$
In vivo electrochemistry
AD

ABSTRACT

The superoxide anion ($O_2^{\bullet -}$) is an important reactive oxygen species (ROS) in the brain system, which has been associated with the development of many neurological diseases, including Alzheimer's disease (AD). Herein, we introduced a carbon fiber microelectrode (CFME) based *in vivo* technique for specific and sensitive monitoring of the $O_2^{\bullet -}$ radical in the living brains of both normal and AD model rats. Compared with other reported superoxide dismutase (SOD) electrochemical biosensors, the microsensor presented in our work was featured in the coating of a functionalized ionic liquid polymer (PIL) onto PB nanoparticles (PBNPs) and carbon nanotubes (CNT). It was demonstrated that the cationic and carboxyl-rich PILs provided abundant interaction sites with SOD to prevent enzyme leakage from sensor, which was beneficial for the enhancement of sensitivity. Additionally, CCK-8 assay and autoxidation of pyrogallol tests showed that MCF-7 cells maintained a high viability after incubated with PIL and most of the SOD bioactivity was retained in the presence of PIL, which implied the PIL itself possessed an excellent biocompatibility. These properties allow the sensor to track the fluctuation of $O_2^{\bullet -}$ levels *in vivo* between normal and AD rats. This is the first report on application of functionalized PIL to reveal the $O_2^{\bullet -}$ related pathological process of AD.

1. Introduction

A characteristic hallmark of one of the major neurodegenerative disorders, Alzheimer's disease (AD), is the deposition of the amyloid β peptide (Aβ) in the brain (Villemagne et al., 2018). Both *in vitro* and *in vivo*, the Aβ monomer will self-assemble into higher order structures, including dimers, trimers, tetramers, larger oligomers, and eventually elongated fibrils (Chen et al., 2018). The inhibition of Aβ fibril assembly has therefore been considered a primary therapeutic strategy for neurodegenerative diseases (Zhao et al., 2019; Du et al., 2018). Notwithstanding an accepted clinical practice, the effectiveness of this treatment strategy is always under controversy because of the multifactorial nature of AD and the current lack of an accepted unitary theory on its etiology (Bolognesi et al., 2007). In this context, the effects of extrinsic or environmental factors such as metal ion homeostasis (Han et al., 2017; Cui et al., 2016; Nam et al., 2018; Chen et al., 2017), degeneration of cholinergic neurons (Huang and Fu, 2017; Luo et al., 2018; Mangalath et al., 2017), and superfluous levels of reactive oxygen species (ROS) (Guan et al., 2016; Beck et al., 2016) on Aβ aggregation are all of high interest, which is useful for understanding the pathophysiology and treatment of AD. Among them, Aβ-induced mitochondrial dysfunction through abnormal overproduction of ROS has widely been known to be a possible cause of AD. An excessive generation of these ROS will inevitably lead to a high oxidative stress and cause diseases, such as cancers, acute inflammation-induced injury, and also AD (Yang et al., 2019; Lou et al., 2015; Yao et al., 2018; Zhao et al., 2018).

Until now, most of the interpretations on the relationship between ROS and Aβ are carried out only at cellular level (Li et al., 2013). The exact concentration variations of ROS associated with AD are still unclear, as the level of ROS can only be judged by observing the luminescence intensity with the naked eye. Due to its highly oxidative

---

[*] Corresponding author. Jiangsu Key Laboratory of New Drug Research and Clinical Pharmacy, Xuzhou Medical University, 209 Tongshan Road, Xuzhou, 221004, Jiangsu, PR China.

[**] Corresponding author.

E-mail addresses: yinxx@xzhmu.edu.cn (X. Yin), yyyxzmc@163.com (Y. Yu).

https://doi.org/10.1016/j.bios.2019.111665
Received 12 July 2019; Received in revised form 27 August 2019; Accepted 29 August 2019

activity and functions, the superoxide anion radical ($O_2^{\bullet -}$) is a rather key radical among kinds of ROS (Wei et al., 2018; Liu et al., 2018). Therefore, the quantitative analysis of $O_2^{\bullet -}$ is critical in the early diagnosis and treatment of ROS induced diseases. In the past decade, a number of methods have been reported for the detection of $O_2^{\bullet -}$ level released from living cells by fluorescence spectroscopy (Zhou et al., 2016; Yun et al., 2014), chemiluminescence (Cai et al., 2018a,b,c; Nam and Lee, 2018), electronspin resonance (ESR) spectroscopy (Haseloff et al., 1991; Kaji et al., 2009), and electrochemical sensing (Wang et al., 2012, 2017; Wei et al., 2018). In particular, electrochemical biosensors have received more and more attentions because of their striking advantages in simplicity, selectivity, low instrumental cost, and capability of real-time, sometimes even *in vivo* detection (Gu et al., 2019; Yu et al., 2018). *In vivo* electrochemistry, using tissue-implantable microelectrodes, is a powerful method to monitor extracellular neurochemicals with a high time and space resolution (Li et al., 2016; Zhou et al., 2016; Vitale et al., 2015; Wilson et al., 2018; Zhang et al., 2019; Liu et al., 2017). Several important requirements for *in vivo* applications must be considered in a microsensor configuration, including specificity, stability, and electrode biofouling by molecular components in high concentrations within the physiological medium, which may lead to a decreased sensitivity (Liu et al., 2017). In this sense, an electrode material which provides a promising reaction interface between substrate and sensor, while remaining resistant to fouling, is an important aspect for *in vivo* biosensor development.

Due to its excellent catalytic activity and good redox properties, prussian blue (PB) has widely been used as a mediator for shuttling the electron transfer on electro-chemical biosensors. Nevertheless, PB has the major drawback of poor chemical and electrochemical stability, because of the interaction between its Fe^{3+} ion and OH^- in a neutral aqueous medium (Sitnikova et al., 2011; Li et al., 2015), which substantially decreases its possible use in *in vivo* applications. In this work, we have developed a carbon fiber-based microelectrode (CFME) for monitoring the change of $O_2^{\bullet -}$ levels in AD rat brains. For the electrode modification, one crucial early step is the coating of ionic liquid polymer (PIL) onto PB nanoparticles (PBNPs) and carbon nanotubes (CNT). PIL is a good matrix for enzyme immobilization, which has been confirmed by several oxidase biosensors (Lee et al., 2012; Zhang et al., 2011). On the one hand, the bioactivity of immobilized enzymes can be well maintained on PIL, due to the matrix's excellent biocompatibility. On the other hand, the tunability of functional groups in the structure of PIL makes it suitable for interacting with enzymes, and it therefore inhibits the leakage of enzymes from biosensors. In view of these attractive advantages of PIL, herein, we constructed an $O_2^{\bullet -}$ biosensor using PIL as the stabilizing layer to immobilize SOD, which constituted the most innovative part of our work over other reported $O_2^{\bullet -}$ electrochemical biosensors that also used SOD. Consequently, the real-time measurement of $O_2^{\bullet -}$ release from living cells, as well as *in vivo* biosensing of $O_2^{\bullet -}$ level changes in AD rat brains, with high sensitivity and specificity was realized. Generally speaking, with the help of *in vivo* technique, we have achieved the accurate contents of $O_2^{\bullet -}$ under normal and pathological conditions at the level of whole animal, which shows a tremendous potential application in assessing oxidative stress on AD progress.

2. Materials and methods

2.1. Chemicals and materials

Multi-walled carbon nanotube (CNT) was provided by Nanjing Xianfeng Nanomaterials Technology Co., Ltd. The IL monomer (IL-Br) and cross-linker (BVD) were provided by Tianxiao Yin. The structure of IL-Br was confirmed by mass spectrum (MS) and ^1H NMR (Fig. S1 and Table S1). 2,2′-azobis(2-methylpropionitrile) (AIBN), potassium superoxide (KO_2), hydrogen peroxide (H_2O_2), sodium nitrite ($NaNO_2$) were bought from Aladdin-Reagent Company (Shanghai, China). Tertbutyl hydroperoxide (TBHP) and hypochlorite (NaOCl) were received from Shanghai Macklin Reagent Company (Shanghai, China). Superoxide dismutase (SOD, from bovine erythrocytes), Zymosan A (from *Saccharomyces cerevisiae*), glutaraldehyde (25%), all the amino acids and copper sulfate ($CuSO_4$) were all purchased from Sigma-Aldrich and used without further purification. DMEM medium was purchased from KeyGEN BioTECH (Nanjing). Fetal bovine serum (FBS) was from Thermo Fisher Scientific, USA. Water (≥18 M) used throughout the whole experiment was purified with Millipore system. All other reagents were of at least analytical grade and commercially available.

2.2. Instruments

Scanning electron microscope images (SEM, Hitachi Co. Ltd., Tokyo, Japan) for the morphological analysis of the modified CFME were taken on a field emission gun Hitachi S-4800 scanning electron microscope (operating at 1 kV). X-ray photoelectron spectroscopy (XPS) measurements were performed on an ESCALab 250Xi X-ray photoelectron spectrometer using Al Kα radiation. UV–vis spectra were recorded on a MAPADA UV-6100 spectrophotometer. The fourier infrared spectroscopy (FT-IR) of PIL was determined using a Nicolet model 460 Fourier transform-infrared spectrometer. ^1H NMR and MS spectra were performed on Bruker DMX 400 spectrometer using $SiMe_4$ as an external standard at 25 °C and Agilent 6460 Triple Quad LC/MS (performed on the electrospray ionization (ESI) source interface in positive mode), respectively.

2.3. Fabrication of SOD/PIL/PB/CNT/CFME

The preparation procedure of a bare CFME is displayed fully in the Supporting Information. For fabrication of the SOD/PIL/PB/CNT/CFME, the CFME was sequentially cleaned in acetone, ethanol and distilled water for 3 min, respectively. Then, the surface of CFME was activated by cycling the potential between 0 and 1.6 V in a 1 M H_2SO_4 solution at 0.1 V/s, until a stable cyclic voltammogram was obtained, followed by washing with distilled water three to four times. For the first step modification with CNT, the protruding tip of CFME was immersed in a 1 mg/mL CNT suspension in DMF for 1.5 h, and dried under an infrared lamp. After that, the electrode was carefully rinsed with double distilled water for several times to remove unassembled materials and dried in air. The obtained electrode was denoted as CNT/CFME.

For the following modification of PBNPs on CNT/CFME, the CNT/CFME was immersed in a electrolyte solution containing 2 mM $K_3[Fe(CN)_6]$, 2 mM $FeCl_3$, 0.1 M KCl, and 0.01 M HCl and scanned between −0.4 and 0.6 V for 10 cycles at 0.05 V/s by cyclic voltammetry. In this way, the layer of PBNPs was electrochemically deposited on CNT/CFME. The resultant electrode was cleaned by distilled water and named as PB/CNT/CFME. To introduce more carboxyl groups onto the electrode for SOD immobilization and stabilizing of the PB layer, the PB/CNT/CFME was further immersed in a PIL suspension (diluted from the original PIL by 20 times with DMF) for 4 h and dried under an infrared lamp for 1 h. After that, the electrode was washed with distilled water to remove excel PIL. This kind electrode was named as PIL/PB/CNT/CFME. The PIL-coated electrode was immersed for 6 h in a PBS solution (0.1 M, pH 7.4) containing 10 mM EDC to activate the carboxylic acid groups on the PIL. Next, the EDC-treated PIL/PB/CNT/CFME was incubated in 0.1 M PBS (pH 7.4) containing 4 mg/mL SOD at 4 °C overnight. SOD was immobilized onto the PIL/PB/CNT/CFME *via* the formation of covalent bonds between the –COOH groups on the PIL and the $-NH_2$ groups on the SOD. After being air-dried for 3 h, the prepared electrode was consecutively immersed in 2.5% glutaraldehyde solution for crosslinking for 1.5 h, and 2.5% Nafion for 40 min to protect it against potential fouling interferences. The obtained electrode was dried at room temperature for 2 h, and stored at 4 °C until use, which was denoted as SOD/PIL/PB/CNT/CFME. The schematic

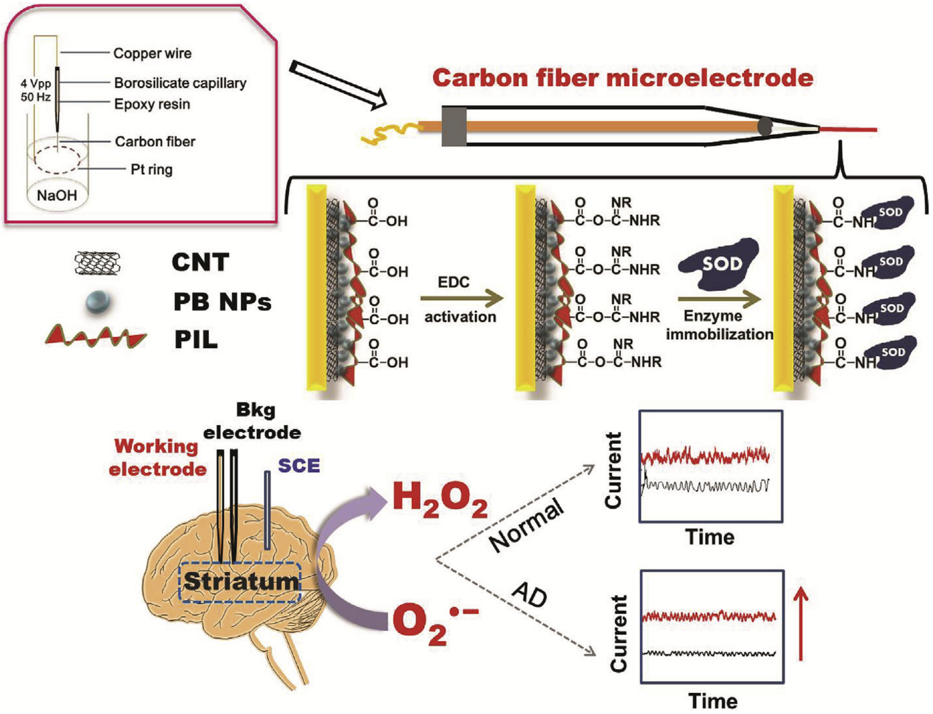

Scheme 1. Schematic diagram showing the fabrication of SOD/PIL/PB/CNT/CFME sensor for the determination of $O_2^{\bullet -}$.

illustration of the fabrication process of SOD/PIL/PB/CNT/CFME was presented in Scheme 1.

2.4. *Cell culture for CCK-8 assay and real time electrochemical detection of cell released $O_2^{\bullet -}$*

The cell culture and CCK-8 assay procedures for this study are shown in the Supporting Information. For real time detection of cell released $O_2^{\bullet -}$ the number of cells was first counted, and all the cells were collected through centrifugation and dispersed in 5 mL aCSF for the electrochemical tests. The amperometric detection of $O_2^{\bullet -}$ released from MCF-7 cells was performed on the SOD/PIL/PB/CNT/CFME electrodes at 0.0 V (*vs.* SCE). Different concentrations of Zymosan were introduced to the cell suspensions to promote the generation of $O_2^{\bullet -}$ when the current reached stable levels, and the current responses were recorded throughout.

2.5. *In vitro and in vivo electrochemical measurements*

Both *in vitro* and *in vivo* electrochemical experiments were carried out on a CHI 832D electrochemical work-station (Chenhua Company, Shanghai) equipped with a shielded box to reduce external electromagnetic interferences on the detected signals. In the *in vitro* measurements, a three-electrode system was used, comprising a bare CFME or SOD/PIL/PB/CNT/CFME as the working electrode, a SCE as the reference electrode, and a platinum wire as the counter electrode. The determination of $O_2^{\bullet -}$ was carried out by immersing the SOD/PIL/PB/CNT/CFME into a 5.0 mL aCSF solution (0.1 M, pH 7.4), and the steady-state currents following consecutive injections of varying amounts of $O_2^{\bullet -}$ were recorded at 0.0 V.

In the *in vivo* experiments, before implanting the CFME into the rat brain to measure the dynamic changes of $O_2^{\bullet -}$ levels, the rats were placed in a stereotaxic frame (Beijing Tide-Gene Biotechnology Development Center) with the incisor bar set at 5 mm above the interaural line, and appropriately placed holes were drilled through the skull. The SOD/PIL/PB/CNT/CFME electrode was implanted in the striatum at the site of 2.4 mm anterior to the bregma, 2.5 mm lateral from the midline, and 4.5 mm below the dura. Electrical contact between brain tissue and a SCE reference electrode was established via a salt bridge fashioned from a plastic pipet tip plugged with tissue paper. All the sensors were calibrated before and after the *in vivo* experiments at ambient temperature. A background CFME was also prepared without SOD and used *in vivo* to obtain an $O_2^{\bullet -}$ - background signal.

3. Results and discussion

3.1. *Confirmation of the SOD/PIL/PB/CNT/CFME fabrication*

The characterizations of the bare CFME are presented in the Supporting Information (Fig. S3). The step-by-step preparation of the SOD/PIL/PB/CNT/CFME was characterized by SEM, XPS, and electrochemical techniques. Fig. 1 displays the SEM images of the surface morphology obtained on the bare CFME, CNT/CFME, PB/CNT/CFME, and SOD/PIL/PB/CNT/CFME. As can be seen, compared with the smooth and unmodified bare CFME (Fig. 1A), a typical three-dimensional tubular microstructure of the uniformly dispersed carbon nanotubes on the surface of the CFME were observed after CNT was casted onto it (Fig. 1B). With further electropolymerization of the PB film to the outer layer of the CNT, the densely distributed PB nanoparticles became clearly visible (Fig. 1C). The good conductivity of the CNT and the large specific surface area of its particular three-dimensional structure provided a suitable platform for the electrodeposition of PB. As PIL and SOD were successively modified to PB/CNT/CFME, as shown in Fig. 1D, a high degree of cross-linking occurred between SOD on the sensor surface and the sensor material, confirming the successful modification of SOD. To further demonstrate the sensor fabrication process, element mapping was investigated (Fig. S4). It could be seen that Fe (a characteristic element of PB), Cu and Zn (characteristic elements of SOD) were successively distributed onto the sensor, indicating the successful modification of PB and SOD.

The surface compositions and chemical oxidation states during the sensor fabrication were characterized by XPS measurement. As displayed in Fig. 2A, prominent peaks at 284.7, 399.9, and 531.5 eV corresponding to C 1s, N 1s, and O 1s were observed on the four spectra.

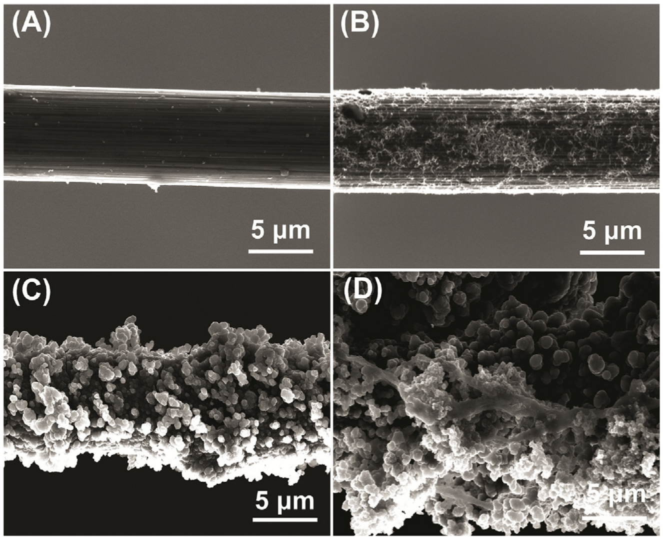

Fig. 1. SEM images of bare CFME (A), CNT/CFME (B), PB/CNT/CFME (C), SOD/PIL/PB/CNT/CFME (D).

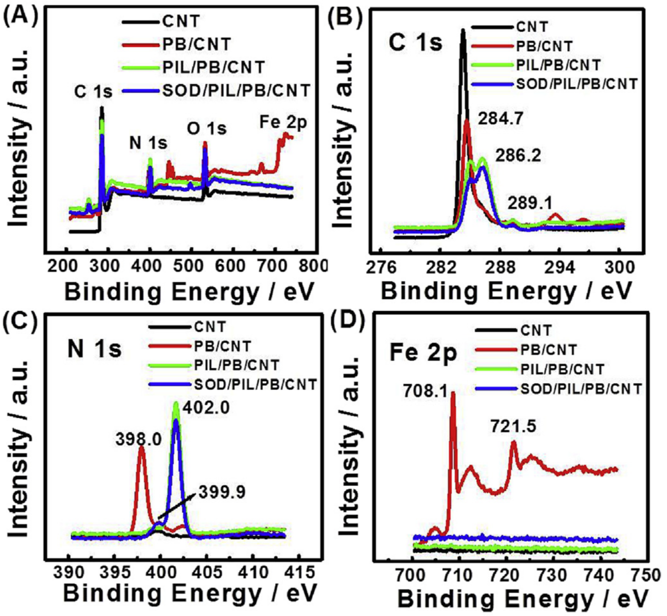

Fig. 2. (A) Peak-fitting XPS survey spectra of CNT, PB/CNT, PIL/PB/CNT and SOD/PIL/PB/CNT. (B–D) The high resolution XPS spectra of C 1s (B), N 1s (C) and Fe 2p (D) on the four composites.

The high-resolution XPS spectra in Fig. 2B–D indicated that with PB modification, two Fe 2p peaks at 708.1 and 721.5 eV and a new N 1s peak at 398.0 eV appeared, which confirmed the presence of PB (Peng et al., 2019). Moreover, following the modification of PIL, the C 1s were separated into three peaks at 284.7, 286.2, and 289.1 eV, indicating three types of C bonds in the PIL structure, which corresponded to C═C/C–C in aromatic rings, C–N, and COOH groups, respectively (Liu et al., 2013). As well, a new higher energy of N 1s appeared at 402.0 eV on the PIL-coated surface, which might be assigned to the tertiary nitrogen (N-(C)$_3$) in the skeleton of PIL (Yu et al., 2017). These results suggested the successful immobilizations of these molecules onto the CFME.

We also used the cyclic voltammetry of $K_3Fe(CN)_6$ to track the sensor modifications. Fig. S5 displays the current changes throughout the layer-by-layer assembly in a $K_3Fe(CN)_6$ solution among the four electrodes, i.e., bare CFME, CNT/CFME, PB/CNT/CFME, and SOD/PIL/PB/CNT/CFME. The bare CFNE exhibited a steady-state voltammogram with a well-defined sigmoidal shape and rather small charging currents. After CNT and PB were stepwise dip-casted onto it, the currents increased significantly. Later on, the currents again decreased significantly when PIL and SOD were modified onto the surface, due to their intrinsically poor conductivities.

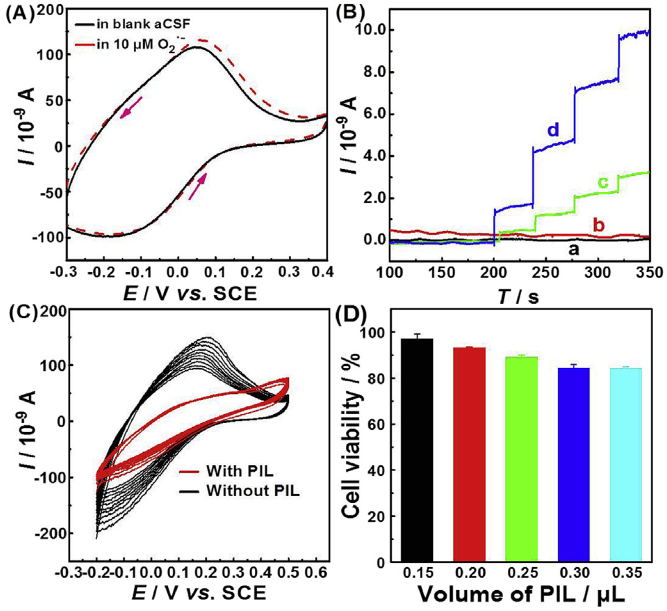

Fig. 3. (A) CV responses of SOD/PIL/PB/CNT/CFME in blank aCSF solution (solid line) and 10 μM $O_2^{\bullet-}$ (dashed line). (B) Amperometric curves of CNT/CFME (a), PB/CNT/CFME (b), SOD/PB/CNT/CFME (c) and SOD/PIL/PB/CNT/CFME (d) toward 10 μM $O_2^{\bullet-}$. Applied potential: 0.0 V. (C) Comparison of CV curves between SOD/PIL/PB/CNT/CFME (red) and SOD/PB/CNT/CFME (black) in 0.1 M aCSF solution scanned for 20 cycles. (D) Cell viability of MCF-7 incubated with different volumes of PIL for 24 h. (For interpretation of the references to colour in this figure legend, the reader is referred to the Web version of this article.)

Since all results from SEM, XPS and CV characterizations were in good agreement with one other, we concluded that these results jointly certificated that the modification strategy for fabricating the SOD/PIL/PB/CNT/CFME sensor was feasible, and had been successful in this case.

3.2. In vitro $O_2^{\bullet-}$ determination by SOD/PIL/PB/CNT/CFME

Before the *in vivo* experiments, the response of the $O_2^{\bullet-}$ sensor was checked in an *in vitro* system. Fig. 3A presents the CV curves of SOD/PIL/PB/CNT/CFME in the absence and presence of 10 μM $O_2^{\bullet-}$ between −0.3 and 0.4 V. When the CV was recorded in a blank aCSF solution, a pair of redox peaks was clearly observed in the potential range of 0.1 ~ −0.2 V, which corresponds to the reduction and oxidation processes of PB. However, compared with the cathodic peak, the anodic peak of the PB was more irregular, which may have been caused by the multiple coatings of poorly conductive compounds over the PB layer. When 10 μM $O_2^{\bullet-}$ was introduced into the 0.1 M aCSF, an obvious increase in the cathodic current was observed, while the anodic current was almost unchanged. The reaction of $O_2^{\bullet-}$ in the experiment could be explained according to the following equation (Lian et al., 2017):

$$2O_2^{\bullet-} + 2H^+ \rightarrow H_2O_2 + O_2$$

Firstly, SOD was able to catalyze the dismutation of $O_2^{\bullet-}$ to O_2 and H_2O_2 via a redox cycle of the copper complex moiety. Then, the generated H_2O_2 was reduced on the electrode by the confined electroactive PB. Accordingly, by measuring the reduction currents of H_2O_2, we were able to detect $O_2^{\bullet-}$ by the SOD/PIL/PB/CNT/CFME. The reduction peak at around 0.05 V was found to be more positive than previous reports on $O_2^{\bullet -}$ detection. The significant positive shift in the reduction potential was indicative of the excellent electrocatalytic activity of CNT and PB toward H_2O_2 reduction.

The optimal working potential was selected at 0.0 V (see Fig. S6). We then investigated and compared the current responses obtained on the four sensors, i.e., CNT/CFME, PB/CNT/CFME, SOD/PB/CNT/CFME, and SOD/PIL/PB/CNT/CFME, toward the same concentration of $O_2^{\bullet -}$, using a chronoamperometric technique. As Fig. 3B shows, compared with curves c and d, with four successive additions of 10 μM $O_2^{\bullet -}$ standard solutions into aCSF, no obvious cathodic currents of $O_2^{\bullet -}$ were generated on the CNT/CFME and PB/CNT/CFME that without SOD modifications (curves a and b). On the other hand, when SOD was modified onto the PB/CNT/CFME electrode surface, a significant catalytic current was observed, which was approximately 0.69 nA for 10 μM $O_2^{\bullet -}$ (curve c). These results confirmed that the presence of the $O_2^{\bullet -}$ reduction current was due to the specific recognition and response by SOD on the electrode surface. Meanwhile, the comparison between curves c and d demonstrated that the catalytic ability of the sensor modified with PIL was higher than that without PIL, with a current enhancement of ~4.4 times. The improved catalytic ability toward $O_2^{\bullet -}$ was therefore concluded to be a result of the addition of PIL. On the one hand, the PIL was rich in positive charges, which may have allowed it to interact with negatively charged PB through electrostatic attractions, so as to stabilize the PB film and retain its electrocatalytic activity. This conclusion is supported by Fig. 3C, where it can be seen that without PIL modification, the peak current of PB continuously decreased with the increase of scanning cycles, and there seemed no stable trend. In comparison, when PIL was modified onto PB, the dropping rate of the peak current was greatly reduced and the current tended to be stable at the 5th cycle. On the other hand, the PIL was also rich in carboxyl groups, which provided enough covalent binding sites with the amine groups of the enzyme, and consequently allowed for the immobilization of sufficient amounts of the enzyme on the sensor. More importantly, PIL was quite different from other polymers in that it had an enhanced biocompatibility, so it would not damage the biological activity of biological macromolecules such as enzymes, which was of great significance for the construction and application of an enzyme-based electrochemical sensor. To verify the applicability of PIL in *in vivo* determination, several additional experiments were conducted. Firstly, we examined the cytotoxicity of PIL by a CCK-8 assay. The results shown in Fig. 3D indicate that with an increase in the incubated volume of PIL, the viability of MCF-7 cells declined gradually but slightly. Even at a high concentration of PIL, the cell viability was still high enough, indicating that PIL had low toxicity to cells. Moreover, we also tested the influence of PIL on the bioactivity of SOD by determining the ability of SOD to inhibit the autoxidation of pyrogallol (Lian et al., 2017). As Fig. S7 shows, only a rather tiny drop in SOD enzyme activity was seen in the presence of PIL, which implied that PIL could be a potential reliable platform for bioactivity analysis.

The amperometric responses of $O_2^{\bullet -}$ on SOD/PIL/PB/CNT/CFME were evaluated using $O_2^{\bullet -}$ standard solutions. As Fig. 4A shows, the catalytic reduction currents rose steeply to a stable value as soon as the standard solutions were introduced into aCSF. The constructed sensor exhibited a good linear relationship toward $O_2^{\bullet -}$ in the range of 1.0–228.0 μM (inset graph). The linear dependency of $O_2^{\bullet -}$ concentration yielded the regression equation of I/nA = (1.55 ± 0.43) + (0.09 ± 0.004) C/μM ($R^2 = 0.99$), with a sensitivity of (0.89 ± 0.04) nA/μM (n = 3). The detection and quantification limits were estimated to be 0.42 and 1.2 μM, which were found be equal to or lower than other reported $O_2^{\bullet -}$ electrochemical biosensors (Crulhas et al., 2017; Cai et al., 2018a,b,c, 2018; Braik et al., 2016; Wang et al., 2012).

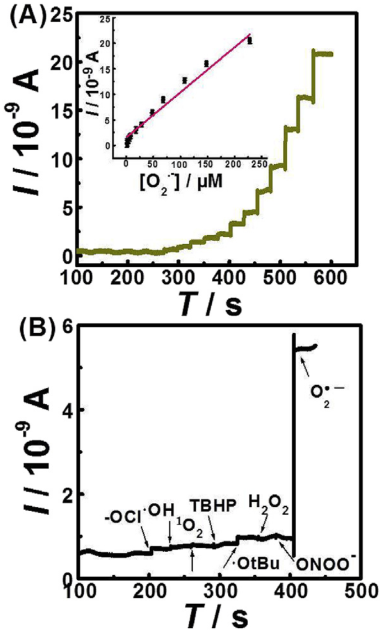

Fig. 4. (A) Amperometric i-t curves on the SOD/PIL/PB/CNT/CFME in aCSF upon successive additions of different concentrations of $O_2^{\bullet -}$. The concentrations of $O_2^{\bullet -}$ were: 1.0, 2.0, 4.0, 6.0, 8.0, 18.0, 28.0, 48.0, 68.0, 108.0, 148.0, 228.0 μM. Inset graph was the fitted linear plot. (B) Selectivity investigation against various endogenic substances *in vivo*. Working potential: 0.0 V.

Besides $O_2^{\bullet -}$, oxidative stress *in vivo* also produces a series of other free radical products. So in order to apply this approach to the specific determination of $O_2^{\bullet -}$ in a rat brain, the selectivity of this assay was examined by adding potential interfering substances (mainly ROS) into aCSF, and determining its current responses in the same way as $O_2^{\bullet -}$. Fig. 4B shows the current responses of SOD/PIL/PB/CNT/CFME with successive additions of $^1O_2$, TBHP, −OCl, •OH, •OtBu, $ONOO^-$, and H_2O_2 in a 0.1 M aCSF (pH 7.4) solution, at an applied potential of 0.0 V. Compared with $O_2^{\bullet -}$, almost no obvious amperometric responses were observed for any of the other species, suggesting that the presence of these species did not affect the detection of $O_2^{\bullet -}$, as a result of the excellent specificity of SOD toward $O_2^{\bullet -}$. This high selectivity provided strong support for our subsequent *in vivo* experiments.

Additionally, to inspect the stability of the microsensor, the sensor was immediately stored at 4 °C for one week after it had been used for determining 10 μM $O_2^{\bullet -}$ once. We found that 92.5% of the original currents were retained after this period, indicating a satisfactory stability of the modified sensor. Five sensors with the same concentration of $O_2^{\bullet -}$ were fabricated in parallel on the same day and consecutively for five days, respectively, and the corresponding amperometric responses were recorded. The two relative standard deviations (RSDs) representing the intra- and inter-precisions were calculated to be 8.68% and 8.52%, respectively. This indicated that the constructed SOD/PIL/PB/CNT/CFME has excellent stability, reproducibility, and repeatability toward $O_2^{\bullet -}$ monitoring.

3.3. Investigation of the kinetic process of $O_2^{\bullet -}$ release from living cells

The applicability of the SOD/PIL/PB/CNT/CFME was initially examined by real time monitoring of the $O_2^{\bullet -}$ release from MCF-7 cells. Zymosan was chosen as the functional drug to stimulate living cells to release molecular $O_2^{\bullet -}$. Fig. S8 shows the current responses obtained on the SOD/PIL/PB/CNT/CFME at 0.0 V, in different conditions. Smooth current baselines were obtained in both PBS and cell suspensions (curves a and b). However, compared with in PBS (curve a), the currents produced in MCF-7 cell suspensions (curve b) were much higher, which indicated that MCF-7 cells released $O_2^{\bullet -}$ constantly and could be detected by our sensor with a fairly high sensitivity. Meanwhile, obvious responses toward the cell-released $O_2^{\bullet -}$ with stable current steps, upon the additions of varying amounts of Zymosan, were observed on

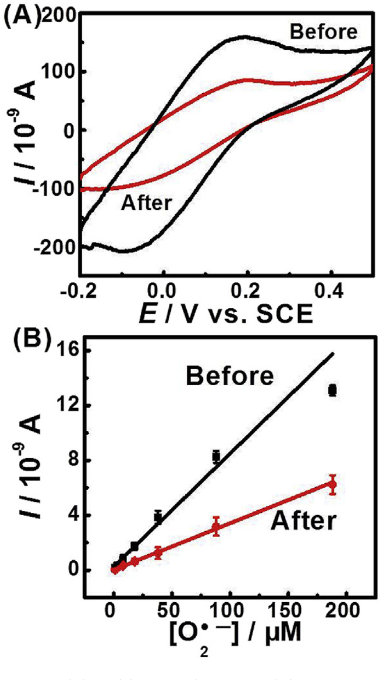

Fig. 5. CV curves (A) and fitted linear plots (B) of the SOD/PIL/PB/CNT/CFME in 0.1 M aCSF solution before (black) and after (red) implanted into rat striatum. Working potential: 0.0 V. (For interpretation of the references to colour in this figure legend, the reader is referred to the Web version of this article.)

the SOD/PIL/PB/CNT/CFME (curves c and d). In both two cases, the current first increased rapidly to a maximum, then decreased gradually, implying that $O_2^{\bullet-}$ in the cells was generated rather quickly following stimulation by Zymosan. Contrary to this, when Zymosan and SOD were added into the above MCF-7 cell suspension simultaneously (curve e), the current changes were fairly weak relative to that in curve d, which meant that the cell-released $O_2^{\bullet-}$ has been scavenged by SOD. These results confirmed that our sensor was fully capable of responding to $O_2^{\bullet-}$ in a cellular matrix with a high sensitivity.

3.4. Performance comparison of SOD/PIL/PB/CNT/CFME on $O_2^{\bullet-}$ before and after in vivo experiments

In the application of microelectrodes *in vivo*, one of the most important problems is the adsorption of proteins onto the surfaces of the electrodes, which leads to the "pollution" of the electrodes, and decreases in their sensitivities. Therefore, we compared the sensor performances before and after implanting into a rat brain, which was carried out with the introduction of various concentrations of $O_2^{\bullet-}$ standard solutions. As shown in Fig. 5A, both oxidation and reduction currents were remarkably reduced after the sensor had been implanted *in vivo* for some time. Moreover, the CV curve also changed significantly, with a far more irregular voltammetry being obtained in the later measurements (curve b). The oxidative peak was clearly broadened and the reductive one was almost eliminated. In order to characterize the degree of decline in the sensitivity of the sensor after implantation in the brain more accurately, we further adopted an amperometric technique to compare the response values of the sensor toward the same concentration of $O_2^{\bullet-}$ before and after implantation in the brain. The results shown in Fig. 5B indicate that after *in vivo* experiments, the current values toward the same concentration of $O_2^{\bullet-}$ in the range of 1.0–188.0 μM were about one-third of those before the implantation. The inset graph shows the two linear standard curves fitted under the two situations, from which the equations were I/nA = (0.07 ± 0.004) C/μM + (0.14 ± 0.14) (precalibration), and I/nA = (0.03 ± 0.001) C/μM + (0.01 ± 0.01) (procalibration), respectively. It can therefore be concluded that during our *in vivo* experiments, the sensitivity of the SOD/PIL/PB/CNT/CFME sensor toward $O_2^{\bullet-}$ decreased by about ~60%. This significant decline in the sensitivity is a common phenomenon for implanted microsensors, which is attributed to the "fouling" of the sensor surface, decreasing the permeabilities of the added modification layers (Sitnikova et al., 2011; Kulagina et al., 1999). Even in such a case, the sensitivity calculated according to post-calibration of the SOD/PIL/PB/CNT/CFME sensor was still high enough to monitor $O_2^{\bullet-}$ variations *in vivo*.

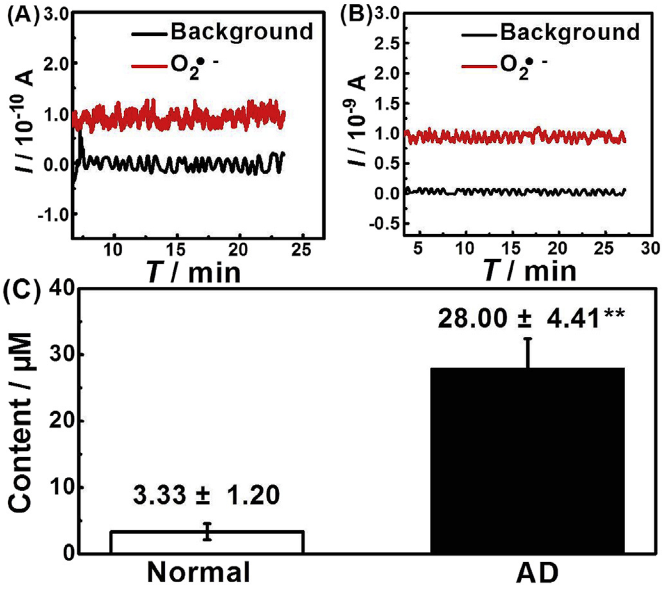

Fig. 6. Amperometric i-t curves of the SOD/PIL/PB/CNT/CFME and a background sensor co-implanted into striatum of normal (A) and AD (B) rats. (C) The post-calculated contents of $O_2^{\bullet-}$ according to the results of A and B.

3.5. In vivo responses of SOD/PIL/PB/CNT/CFME and background sensors

Fig. 6A–B presents the typical current responses recorded from the SOD/PIL/PB/CNT/CFME and another background microsensor simultaneously, which were implanted side-by-side in the striatum of both normal and AD rat brains. As indicated from these i-t curves, the stable baseline signals obtained on the SOD/PIL/PB/CNT/CFME were higher than that of the background microsensor throughout the experiment, which was likely due to the electrochemical reduction of $O_2^{\bullet-}$ in the presence of SOD. Based on the post-calibrated sensitivity after *in vivo* experiments, the constant difference in their baseline signals was found to be associated with a basal $O_2^{\bullet-}$ concentration of 3.33 ± 1.20 μM in normal rat brains (n = 3). A clear rise in this value up to 28.00 ± 4.41 μM (n = 3) was witnessed in the striatum of AD rats ($P < 0.01$). It has been widely acknowledged that the binding of Aβ to metal ions makes Aβ deposit in brain and contribute to the production of neurotoxic ROS, including $O_2^{\bullet-}$. Continuously increasing levels of $O_2^{\bullet-}$, along with Aβ aggregation, triggers a series of damages to cellular components such as DNA, lipids, and proteins (Yang et al., 2016). However, most studies on this increase in $O_2^{\bullet-}$ production have been based on various qualitative techniques, and therefore the accurate concentrations of this free radical involved in the pathological and physiological process of AD have remained unclear thus far. The developed SOD/PIL/PB/CNT/CFME sensor showed high sensitivity and specificity toward $O_2^{\bullet-}$ determination, and demonstrated its ability to track the change of $O_2^{\bullet-}$ levels associated with AD both *in vitro* and *in vivo*.

4. Conclusions

In summary, an $O_2^{\bullet -}$ microsensor based on SOD immobilized on a PIL matrix was fabricated for the *in vivo* measurement of $O_2^{\bullet -}$ in living brains of rats. Besides a low toxicity of the PIL itself, the incorporation of PIL not only stabilized the PB film and retained its electrocatalytic activity, but also allowed for the immobilization of sufficient amounts of SOD onto the sensor, to enhance its sensitivity and stability to low $O_2^{\bullet -}$ concentrations. Thus, the sensor had the ability to track the $O_2^{\bullet -}$ level variations in normal and pathological conditions of a living brain system. We believe that this $O_2^{\bullet -}$ microsensor could be an effective tool to facilitate msore discoveries on the relationship between oxidative stress and the brain.

CRediT authorship contribution statement

Qiwen Peng: Methodology, Validation, Writing - original draft, Writing - review & editing. **Xueyan Yan:** Validation, Software, Writing - original draft. **Xinran Shi:** Software, Writing - original draft. **Shanshan Ou:** Investigation. **Hui Gu:** Supervision. **Xiaoxing Yin:** Supervision, Project administration. **Guoyue Shi:** Funding acquisition, Supervision. **Yanyan Yu:** Funding acquisition, Project administration, Writing - review & editing, Resources.

Declaration of competing interest

The authors declare that they have no known competing financial interests or personal relationships that could have appeared to influence the work reported in this paper.

Acknowledgement

This work was financially supported by the National Natural Science Foundation of China (no. 21675137), Natural Science Foundation of Jiangsu Province (no. BK20161170), Natural Science Foundation of Jiangsu Higher Education Institute of China (no. 17KJA350004), Program for Distinguished Talents of Six Domains in Jiangsu Province (no. 2016-SWXY-060), Jiangsu "333" project of cultivation of high-level talents (no. BRA2016458) and Jiangsu Overseas Visiting Scholar Program for University Prominent Young & Middle-aged Teachers and Presidents.

Appendix A. Supplementary data

Supplementary data to this article can be found online at https://doi.org/10.1016/j.bios.2019.111665.

References

Beck, M.W., Derrick, J.S., Kerr, R.A., Oh, S.B., Cho, W.J., Lee, S.J.C., Ji, Y., Han, J., Tehrani, Z.A., Suh, N., Kim, S., Larsen, S.D., Kim, K.S., Lee, J.-Y., Ruotolo, B.T., Lim, M.H., 2016. Nat. Commun. 7, 13115–13128.
Bolognesi, M.L., Cavalli, A., Valgimigli, L., Bartolini, M., Rosini, M., Andrisano, V., Recanatini, M., Melchiorre, C., 2007. J. Med. Chem. 50, 6446–6449.
Braik, M., Barsan, M.M., Dridi, C., Ben Ali, M., Brett, C.M.A., 2016. Sens. Actuators B Chem. 236, 574–582.
Cai, L.P., Deng, L.Y., Huang, X.Y., Ren, J.C., 2018a. Anal. Chem. 6929–6935.
Cai, X., Shi, L.B., Sun, W.Q., Zhao, H.L., Li, H., He, H.Y., Lan, M.B., 2018b. Biosens. Bioelectron. 102, 171–178.
Cai, X., Shi, L.B., Zhao, H.L., Lan, M.B., 2018c. Chemnanomat 4, 213–219.
Chen, Q., Du, Y., Zhang, K., Liang, Z.Y., Li, J.Q., Yu, H., Ren, R., Feng, J., Jin, Z.M., Li, F.Y., Sun, J.H., Zhou, M., He, Q.G., Sun, X.L., Zhang, Tian, M., Ling, D.S., 2018. ACS Nano 12, 1321–1338.
Chen, W.S., Ouyang, J., Yi, X.Y., Xu, Y., Niu, C.C., Zhang, W.Y., Wang, L.Q., Sheng, J.P., Deng, L., Liu, Y.N., Guo, S.J., 2017. Adv. Mater 1703458-1703465.
Crulhas, B.P., Recco, L.C., Delella, F.K., Pedrosa, V.A., 2017. Electroanalysis 29, 1252–1257.
Cui, Z.W., Bu, W.B., Fan, W.P., Zhang, J.W., Ni, D.L., Liu, Y.Y., Wang, J., Liu, J.N., Yao, Z.W., Shi, J.L., 2016. Biomaterials 104, 158–167.
Du, Z., Gao, N., Wang, X.H., Ren, J.S., Qu, X.G., 2018. Small 14, 1801852–1801859.
Gu, H., Hou, Q., Liu, Y., Cai, Y.J., Guo, Y.Q., Xiang, H.Y., Chen, S., 2019. Biosens. Bioelectron. 135, 111–119.
Guan, Y.J., Gao, N., Ren, J.S., Qu, X.G., 2016. Chem. Eur J. 22, 14523–14526.
Han, Qi S., Cai, S.F., Yang, L., Wang, X.H., Qi, C., Yang, R., Wang, C., 2017. ACS Appl. Int. Mater. 9, 21116–21123.
Haseloff, R.F., Ebert, B., Wischnewsky, G.G., 1991. Anal. Chim. Acta 243, 221–225.
Huang, S.Y., Fu, W.M., 2017. J. Biomed. Sci. 24, 47–59.
Kaji, H., Inukai, Y., Maiguma, T., Ono, H., Teshima, D., Hiramoto, K., Makino, K., 2009. J. Clin. Pharm. Ther. 34, 197–205.
Kulagina, N.V., Shankar, L., Michael, A.C., 1999. Anal. Chem. 71, 5093–5100.
Lee, S., Ringstrand, B.S., Stone, D.A., Firestone, M.A., 2012. ACS Appl. Mater. Interfaces 4, 2311–2317.
Li, R., Guo, D., Ye, J., Zhang, M., 2015. Analyst 140, 3746–3752.
Li, M., Shi, P., Xu, C., Ren, J.S., Qu, X.G., 2013. Chem. Sci. 4, 2536–2542.
Li, R.X., Liu, X.M., Qui, W.L., Zhang, M.N., 2016. Anal. Chem. 88, 7769–7776.
Lian, M.L., Xu, L., Zhu, X.W., Chen, X., Yang, W.S., Wang, T., 2017. Anal. Chem. 89, 12843–12849.
Liu, J.J., Zhang, X.L., Cong, Z.X., Chen, Z.T., Yang, H.H., Chen, G.N., 2013. Nanoscale 5, 1810–1815.
Liu, R.J., Zhang, L.L., Chen, Y.Y., Huang, Z.R., Huang, Y., Zhao, S.L., 2018. Anal. Chem. 90, 4452–4460.
Liu, X.M., Xiao, T.F., Wu, F., Shen, M.Y., Zhang, M.N., Yu, H.H., Mao, L.Q., 2017. Angew. Chem. Int. Ed. 56, 11802–11806.
Lou, Z.R., Li, P., Han, K.L., 2015. Accounts Chem. Res. 48, 1358–1368.
Luo, Y., Kim, E.H., Flask, C.A., Clark, H.A., 2018. ACS Nano 12, 5761–5773.
Mangalath, S., Abraham, S., Joseph, J., 2017. Chem. Eur J. 23, 11404–11409.
Nam, E., Derrick, J.S., Lee, S., Kang, J., Han, J., Lee, S.J.C., Chung, S.W., Lim, M.H., 2018. ACS Chem. Neurosci. 2655–2666.
Nam, S.J., Lee, W.Y., 2018. J. Electroanal. Chem. 808, 59–64.
Peng, Z., Qiu, X.Y., Yu, Y., Jiang, D., Wang, H.T., Cai, G.Y., Zhang, X.X., Dong, Z.H., 2019. Carbon 152, 16–23.
Sitnikova, N.A., Borisova, A.V., Komkova, M.A., Karyakin, A.A., 2011. Anal. Chem. 83, 2359–2363.
Villemagne, V.L., Doré, V., Burnham, S.C., Masters, C.L., Rowe, C.C., 2018. Nat. Rev. 14, 225–236.
Vitale, F., Summerson, S.R., Aazhang, B., Kemere, C., Pasquali, M., 2015. ACS Nano 9, 4465–4474.
Wang, M.Q., Ye, C., Bao, S.J., Xu, M.W., Zhang, Y., Wang, L., Ma, X.Q., Guo, J., Li, C.M., 2017. Biosens. Bioelectron. 87, 998–1004.
Wang, X.H., Han, M., Bao, J.C., Tu, W.W., Dai, Z.H., 2012. Anal. Chim. Acta 717, 61–66.
Wei, H.W., Shang, T.Y., Wu, T.D., Liu, G.A., Ding, L., Liu, X.H., 2018. Biosens. Bioelectron. 100, 8–15.
Wilson, L.R., Panda, S., Schmidt, A.C., Sombers, L.A., 2018. Anal. Chem. 90, 888–895.
Yang, L.C., Yin, T.T., Liu, Y.A., Sun, J., Zhou, Y.H., Liu, J., 2016. Acta Biomater. 46, 177–190.
Yang, Y., Wang, L., Cao, H.Q., Li, Q., Li, Y., Han, M.J., Wang, H., Li, J.B., 2019. Nano Lett. 19, 1821–1826.
Yao, J., Cheng, Y., Zhou, M., Zhao, S., Lin, S.C., Wang, X.Y., Wu, J.J.X., Li, S.R., Wei, H., 2018. Chem. Sci. 9, 2927–2933.
Yu, Y.Y., Wang, P., Zhu, X.D., Peng, Q.W., Zhou, Y., Yin, T.X., Liang, Y.X., Yin, X.X., 2018. Analyst 143, 323–331.
Yu, Y.Y., Yu, C., Yin, T.X., Ou, S.S., Sun, X.Y., Wen, X.R., Zhang, L., Tang, D.Q., Yin, X.X., 2017. Biosens. Bioelectron. 87, 278–284.
Yun, S.W., Kang, N.Y., Park, S.J., Ha, H.H., Kim, Y.K., Lee, J.S., Chang, Y.T., 2014. Accounts Chem. Res. 47, 1277–1286.
Zhang, D., Ma, J.J., Meng, X.W., Xu, Z.F., Zhang, J., Fang, Y.X., Guo, Y., 2019. Anal. Chim. Acta 1076, 55–63.
Zhang, Q., Wu, S.Y., Zhang, L., Lu, J., Verproot, F., Liu, Y., Xing, Z.Q., Li, J.H., Song, X.M., 2011. Biosens. Bioelectron. 26, 2632–2637.
Zhao, H., Zeng, Z.D., Liu, L., Chen, J.W., Zhou, H.T., Huang, L.L., Huang, J., Xu, H., Xu, Y.Y., Chen, Z.G., Wu, Y., Guo, W.L., Wang, J.H., Wang, J., Liu, Z., 2018. Nanoscale 10, 6981–6991.
Zhao, Y., Cai, J.Q., Liu, Z.C., Li, Y.S., Zheng, C.X., Zheng, Y.D., Chen, Q., Chen, H.Y., Ma, F.H., An, Y.L., Xiao, L.H., Jiang, C.L., Shi, L.Q., Kang, C.S., Liu, Y., 2019. Nano Lett. 19, 674–683.
Zhou, Y., Ding, J., Liang, T.X.Z., Abdel-Halim, E.S., Jiang, L.P., Zhu, J.J., 2016. ACS Appl. Mater. Interfaces 8, 6423–6430.